Materials Today Bio 26 (2024) 101083

Contents lists available at ScienceDirect

Materials Today Bio

journal homepage: www.journals.elsevier.com/materials-today-bio

Electrowriting patterns and electric field harness directional cell migration for skin wound healing

Huinan Lai [a,1], Xiaodan Huo [b,1], Ying Han [b], Minyu Hu [a], Xiangren Kong [a], Jun Yin [b,*], Jin Qian [a,b,**]

[a] Department of Engineering Mechanics, Key Laboratory of Soft Machines and Smart Devices of Zhejiang Province, Zhejiang University, Hangzhou, China
[b] The State Key Laboratory of Fluid Power Transmission and Control Systems, Key Laboratory of 3D Printing Process and Equipment of Zhejiang Province, School of Mechanical Engineering, Zhejiang University, Hangzhou, China

ARTICLE INFO

Keywords:
Cell migration
Electrical stimulation
Topographic cues
Solution electrowriting
Wound healing

ABSTRACT

Directional cell migration is a crucial step in wound healing, influenced by electrical and topographic stimulations. However, the underlying mechanism and the combined effects of these two factors on cell migration remain unclear. This study explores cell migration under various combinations of guided straight line (SL) spacing, conductivity, and the relative direction of electric field (EF) and SL. Electrowriting is employed to fabricate conductive (multiwalled carbon nanotube/polycaprolactone (PCL)) and nonconductive (PCL) SL, with narrow (50 μm) and wide (400 μm) spacing that controls the topographic stimulation strength. Results show that various combinations of electrical and topographic stimulation yield significantly distinct effects on cell migration direction and speed; cells migrate fastest with the most directivity in the case of conductive, narrow-spacing SL parallel to EF. A physical model based on intercellular interactions is developed to capture the underlying mechanism of cell migration under SL and EF stimulations, in agreement with experimental observations. *In vivo* skin wound healing assay further confirmed that the combination of EF (1 V cm^{-1}) and parallelly aligned conductive fibers accelerated the wound healing process. This study presents a promising approach to direct cell migration and enhance wound healing by optimizing synergistic electrical and topographic stimulations.

1. Introduction

Skin, the largest organ of the human body, acts as a protective barrier against harmful external factors and pathogens [1,2]. Enhancing the wound healing rate is crucial to prevent potentially fatal consequences in severe skin injury cases [3,4]. Cell migration is an important step in skin wound healing, involving various cell types, such as epithelial cells, keratinocytes, fibroblasts, vascular endothelial cells, inflammatory cells, and so on [5]. Cell migration is primarily regulated by the endogenous bioelectric field and extracellular matrix topography [6–10]. Thus, the interplay among the electric field (EF), substrate topography, and cell migration is vital to develop promising strategies for accelerating skin wound healing. The influence of electrical and topographic factors on cell migration is often studied separately in the literature.

Progresses have been made in investigating the individual effect of electrical stimulation on cell migration. It has been revealed that EF can enhance cell migration speed, and guide directional cell migration, which is known as electrotaxis [11,12]. Interestingly, different cell types exhibit distinct preferences in directional migration under an EF: dermal fibroblasts, Schwann cells, breast cancer cells, and lung adenocarcinoma cell lines migrate toward the anode, whereas keratinocytes, mouse embryo fibroblasts, Xenopus neurons, and rat 3T3 fibroblasts migrate toward the cathode [13].

Moreover, there are some studies investigating cell migration under the influence of substrate topography. For substrate topography, the effects of discrete and continuous structures on cell migration have been investigated [14]. Discrete structures, mainly pillars with various shapes and sizes from tens of nanometers to microns, can significantly change

* Corresponding author.
** Corresponding author. Department of Engineering Mechanics, Key Laboratory of Soft Machines and Smart Devices of Zhejiang Province, Zhejiang University, Hangzhou, China.
E-mail addresses: junyin@zju.edu.cn (J. Yin), jqian@zju.edu.cn (J. Qian).
[1] These authors contributed equally to this work.

https://doi.org/10.1016/j.mtbio.2024.101083
Received 25 January 2024; Received in revised form 20 April 2024; Accepted 3 May 2024
Available online 6 May 2024

the cell migration speed [15,16]. Continuous structures of grooves and fibers, with a scale ranging from tens of nanometers to hundreds of microns, can influence the cell migration direction and speed [17–19]. It is worth noting that cells usually encounter fibrous, continuous structures when migrating *in vivo*, so exploring cell migration on continuous fibrous structures makes more sense [20]. To manufacture such microscale and nanoscale continuous structures, traditional methods, such as photolithography and molding are complex, expensive, and challenging to change dimensionally [21,22]. Electrowriting, which precisely controls fiber deposition through electrostatic force, can fabricate fibers within the desired size range while avoiding the previously mentioned drawbacks [23].

Current studies on the effects of electrical stimulation and geometric patterning on cells mainly focus on the effects on cell differentiation and cell alignment, and there are almost no studies on cell migration [24]. For example, Electric field parallel to the microgrooves can enhance the myogenic maturation of human myogenic precursor cell [25], the cell alignment and elongation of C2C12 myoblasts [26], and promote muscle regeneration. Electric field parallel to the grooves also can enhance proliferation, directional migration and orientation of human dermal fibroblasts [27]. Electric field added to the conductive grid also can affect neurite outgrowth (PC-12 cells and primary mouse hippocampal neurons) and the formation of orientated neuronal-like networks [28]. However, in the above study, the electric field is simply applied to the conducting geometric pattern, and the effects of different combinations of guided patterns and electric field direction were not studied. Therefore, the synthetic effects of electrical and topographical factors on cell migration need to be further investigated.

Herein, this study investigated the combined stimulating effects of EF and substrate topography on cell migration (Fig. 1). Conductive (multi-walled carbon nanotubes (MWCNT)/Polycaprolactone (PCL)) and nonconductive (PCL) straight lines (SL) printed by electrowriting with narrow (50 μm) and wide (400 μm) spacing were fabricated as guided substrate topograpshy. Cell migration was characterized under several stimulating configurations, namely, EF alone, SL alone, EF parallel to SL, and EF perpendicular to SL, each with different settings in SL conductivity and spacing. A physical model based on intercellular interaction was developed to capture the underlying mechanism of cell migration under SL and EF stimulations, quantitatively consistent with experimental observations. *In vivo* assay of mouse skin was performed to further confirm the synergistic effects of SL and EF stimulations on wound healing. This study provides useful clues in understanding the synergistic effects of electrical and topographic stimulations on cell migration and has implications for promoting skin wound healing.

2. Materials and methods

2.1. Preparation of MWCNT/PCL ink

Different mass fractions of MWCNT (0, 0.05, 0.1, 0.2, and 0.4 wt%; Suzhou Tanfeng Graphene Technology Co., Ltd, China) were added into dichloromethane (Yonghua Chemical Co., Ltd., China) and homogeneously dispersed by ultrasound for 6 h at 20 °C. PCL (Jinan Daigang Biomaterial Co., Ltd., China) with a molecular weight of 160,000 was added to the dispersant and stirred for 24 h to get homogeneous solutions.

2.2. Characterization of MWCNT/PCL ink

Sheets (2 cm × 2 cm × 5 mm) sheets were manufactured by molding to evaluate the hydrophobicity and conductivity of different MWCNT/PCL ratios (0, 0.05, 0.1, 0.2, and 0.4 wt%). Hydrophobicity was characterized by a contact angle measuring instrument (Dataphysics, Germany). Conductivity was measured by the four-probe resistivity meter (Halpass Electronic Technologies, Co., Ltd., China). The variation of viscosity with the shear rate for different ratios of the MWCNT/PCL solution was tested by a rheometer (Anton Paar, Germany).

2.3. Electrowriting of MWCNT/PCL guided patterns

Solution electrowriting was employed to fabricate MWCNT/PCL (0 and 0.2 wt%) SL with a diameter of 30 μm and with spacings of 50 and 400 μm as cell-guided patterns. The printing ink was filled into a syringe with a stainless-steel nozzle with an inner diameter of 150 μm. The printing ink was extruded at a rate of 0.05 ml h^{-1}. The distance and voltage between the needle and the movable platform were 1 mm and 2 kV, respectively. The moving speed of the platform was 5,000 mm min^{-1}. Printed fibers were deposited on a siliconized glass, which

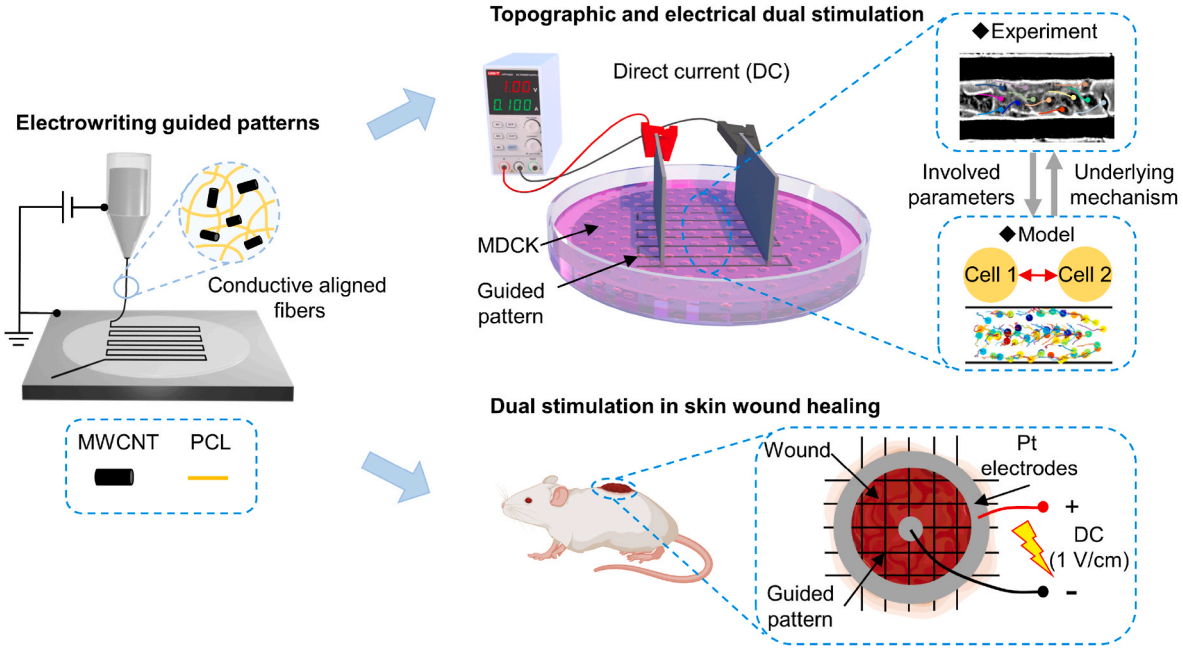

Fig. 1. Schematic diagram of the electrowriting printing guided patterns, topographic and electrical dual stimulation on cell migration and skin wound healing.

offered excellent fiber adhesion. The micromorphology of printed structures was observed by optical microscopy (Leica, Germany) and field emission SEM (GeminiSEM 300; Zeiss, Germany; operated at 10 kV) after sputtering coated with gold.

2.4. Cell seeding in guided patterns

MDCK (Madin-Darby Canine Kidney) cells were cultured in minimum essential medium (Gibco, USA) supplemented with 10 % fetal bovine serum (Gibco) and 1 % penicillin/streptomycin (Gibco), and incubated in a cell incubator (Thermo Fisher Scientific, USA) with 37 °C and 5 % CO_2. Substrates consisting of siliconized glass and printing fibers were fixed into the culture dish with a diameter of 60 mm by Teflon tapes and sterilized by ultraviolet (UV) light for 2 h. MDCK cells were uniformly seeded onto the sterilized substrate at a density of 40,000 cells ml^{-1} $dish^{-1}$.

2.5. Biocompatibility evaluation and cell morphology observation on the MWCNT/PCL substrate

The cytotoxicity of 0 and 0.2 wt% MWCNT/PCL was evaluated by the CCK-8 assay (Beyotime Biotechnology Co., Ltd., China) on days 1, 2, and 3 after culture. Briefly, CCK-8 was diluted by the cell culture medium (9:1), and 2 ml diluent was added to the culture dish. After 30 min incubation in an incubator, 200 μl supernatant was extracted and added to a 96-well plate. Optical density (OD) at 450 nm was measured by a multifunction microplate reader (Thermo Fisher Scientific). Cell proliferation was calculated as the ratio of the OD value measured on the day to the value of the first day.

The cell growth condition was characterized by the cell spread area analyzed based on immunofluorescence images of cytoskeleton staining. Briefly, cells were fixed in 4 % paraformaldehyde (Solarbio, China) for 30 min and permeabilized with 0.5 % Triton X-100 (Solarbio) for 20 min at room temperature. A phalloidin-FITC (1:200; Solarbio) solution was applied for staining the F-actin of cells in the dark for 2 h. Then, DAPI (Solarbio) was used to stain nuclei for 30 min. Finally, all samples were rinsed twice with phosphate-buffered saline (PBS) and observed. The staining samples were observed under inverted phase-contrast fluorescence microscope (Leica). The cell spread area was measured by Fiji/ImageJ (National Institutes of Health, USA), and 50 cells were analyzed in each group.

2.6. Cell migration in EF and guided patterns

EF was added after cells were completely attached to the substrate. The DC power source was connected to Cu wires that protruded from the culture dish by alligator clips to add the predesigned EF. The connected Cu wires and Pt electrodes were fixed vertically on the culture dish lid by polytetrafluoroethylene tape. Pt electrodes were directly inserted into the culture medium. The culture dish was fixed on the time-lapse microscope CytoSMART Lux2 (CytoSMART Technologies, The Netherlands) to monitor cell migration. Microscopy images were taken every 5 min for 2 h and imported into Fiji/ImageJ, extracting the cell displacement. The average cell migration speed was calculated by analyzing 50 cells in each group. The strength of electric field (*EF*) was calculated by the following formula:

$$EF = U/d, \tag{1}$$

where U is the voltage applied between the two parallel electrodes, and d is the distance between the two electrodes. Cell migration speed (v) is calculated by the following formula:

$$v = l/t, \tag{2}$$

where l is the cell migration distance, and t is the time spent by the cell in moving distance l. The cell migration angle (θ) is defined as the angle between the line connecting the starting and ending points of the cell track and the direction of EF. The directionality of cell migration is characterized by cosθ and orientation ratio that is calculated by the following formula:

$$orientation\ ratio = N_{\theta=-45^\circ\sim45^\circ}/N_{\text{total}}, \tag{3}$$

where $N_{\theta=-45^\circ-45^\circ}$ is the number of cells with a migration angle between the 45° above and below the direction of EF, and N_{total} is the total number of cells.

2.7. Finite element analysis of EF distribution in guided SL

To analyze the EF distribution between conductive and nonconductive guided SL in the cell culture medium, 3D finite element models were developed. The finite element models consisted of printing fibers and the cell culture medium, represented by a cylinder and a rectangle, respectively. EF was added to the ends of the cylinder and set as 1 V cm^{-1}. The conductivities of printing fibers and the cell culture medium were assigned according to the experiment data, as shown in Table S1.

2.8. Physical model of cell migration

The compass-based model in the literature was improved as our model to describe and forecast cell migration [29]. In stimulation, cell migration direction is determined by the interaction with surrounding cells, free edge, boundaries, and the EF. Cells repulse each other when the distance between them is less than the cell diameter but attract each other when the distance is greater than the cell diameter and less than thrice the cell diameter, and do not interact with cells that the distance between them is greater than thrice the cell diameter. Based on experimental observations, cells prefer to migrate toward the free edge where no cells exist. To simulate the effects of grooves on cells, a cell-boundary interaction was added, which equates the boundary to the nearest cell interacting with the central cell. The parameters set in the simulations, such as cell diameter, changes in cell migration speed, and orientation due to EF, were obtained experimentally. Moreover, the variation of cell migration speed and orientation ratio with EF were fitted and assigned as the model setup. The parameter setting, calculation method, and program package are described in Tables S2 and SI for details.

2.9. In vivo wound-healing assay

Normal 8-week female ICR mice with an average weight of 30 g (Shanghai Slac River Laboratory Animal Co., Ltd.) were used for the *in vivo* wound-healing assay. Each mouse was anesthetized by inhaling isoflurane through an animal anesthetic machine (Shenzhen Reward Life Technology Co., Ltd., China). The full-thickness rectangular wound (1 × 1 cm) was cut on the back of each mouse. The wounds were divided into four different groups: control (without guided pattern and EF), PCL (nonconductive guided pattern, without EF), MWCNT/PCL (conductive guided pattern, without EF), and MWCNT/PCL + EF groups (conductive guided pattern, with EF). Guided MWCNT/PCL and PCL patterns were fabricated by electrowriting, which were grid membranes with a thickness of 500 μm and a fiber diameter of 50 μm that can induce cells to migrate toward the wound center. All guided membranes were sterilized by UV light for 2 h, and cut into rectangle shapes with a width of 1.5 cm. The wound was directly covered with the membrane. In the EF group, the electrodes were sterilized by UV light and 75 % ethanol, positioned above the membrane, and fixed with medical gauze and tape. EF (1 V cm^{-1}) was applied by annular and circular electrodes connected to the anode and cathode, respectively, to form an EF toward the wound center, and the power was supplied by the button cell. EF was applied for 1 h once daily. The wounds were photographed on days 0, 3, 7, and 14, followed by wound area measurement. The wound closure rate was calculated by the following formula:

$$Wound\ closure\ rate = (A_0 - A_c) / A_0 \times 100\%, \quad (4)$$

where A_0 is the wound area of day 0, and A_c is the current wound area.

2.10. Histology and immunohistochemical analysis

A histopathological evaluation of tissue regeneration was conducted by H&E staining. Before the histological examination, regenerated wound tissues collected on day 14 were fixed with 4 % (w/v) paraformaldehyde, washed with PBS, dehydrated using graded ethanol, embedded in paraffin, and cut into 3-μm-thick cross-sections. Tissue sections were stained and observed using a slide scanner (Pannoramic MIDI, Hungary). Granulation tissue thickness was measured on digital images using ImageJ.

2.11. Statistical analysis

All data were presented as the mean ± standard deviation. Statistical significance was determined using one-way statistical analysis of variance (ANOVA) followed by Tukey's post hoc test for multiple comparisons using Origin (Originpro 2023 learning edition). Differences were considered statistically significant if $p < 0.05$ (*) and $p < 0.01$ (**), and nonstatistically significant if $p > 0.05$ (ns).

3. Results and discussion

3.1. Ink characterization and guided pattern electrowriting

3.1.1. Selecting the optimal ratio of MWCNT/PCL ink

Different ratios of MWCNT/PCL (0, 0.05, 0.1, 0.2, and 0.4 wt%) ink were prepared by sonication and stirring, and PCL concentration was fixed at 0.4 g ml^{-1} resolved in dichloromethane (DCM). The optimal MWCNT/PCL ratio was selected as the conductive material with good cell adhesion, conductivity, and electrowriting printability. These attributes can be evaluated through hydrophilicity, conductivity, and rheological tests, respectively. Different MWCNT/PCL ratios were molded into square sheets to test hydrophilicity (contact angle) and conductivity. Results revealed that the contact angle decreased as the MWCNT ratio increased, and the material became hydrophilic when the ratio reached 0.2 wt% (Fig. 2A). The conductivity increased with increasing MWCNT ratios, and the compound remained nonconductive until the mass fraction of MWCNT reached 0.2 wt% (5 μS cm^{-1}; Fig. 2B). It was adequate to stimulate cells until the substrate conductivity surpassed 1 μS cm^{-1} [30], and the conductivity of stratum corneum was nearly 0.02 μS cm^{-1} [2]. Thus, to achieve the conductivity, the MWCNT ratio must be ≥ 0.2 wt%. Moreover, the variation of viscosity with the shear rate suggested that the viscosity decreased with increasing shear rate for all proportions of MWCNT, and the initial viscosity increased with increasing MWCNT proportions, and 0.4 wt% MWCNT/PCL exhibited excessive viscosity, impeding electric jet formation in electrowriting (Fig. 2C). Therefore, 0.2 wt% MWCNT/PCL was chosen as the conductive material for subsequent experiments considering the need for cell adhesion, conductivity, and printability; hereinafter, MWCNT/PCL was used to represent 0.2 wt% MWCNT/PCL. Also, 0 wt% MWCNT/PCL (pure PCL) was chosen as the nonconductive material; hereinafter, PCL was used to represent 0 wt% MWCNT/PCL.

3.1.2. Electrowriting of MWCNT/PCL and PCL patterns

MWCNT/PCL and PCL patterns were fabricated by electrowriting with the printing parameters mentioned in the Experimental section. A standard electric jet was formed at the tip of the needle (Video S1). The morphology of MWCNT/PCL (Fig. 2D) and PCL (Fig. 2E) fibers were observed using optical microscope and scanning electron microscope. The images revealed that the average fiber diameter was about 30 μm, and fibers stacked well in the height direction. In addition to grid structures, patterns with angles and curves can also be printed, proving

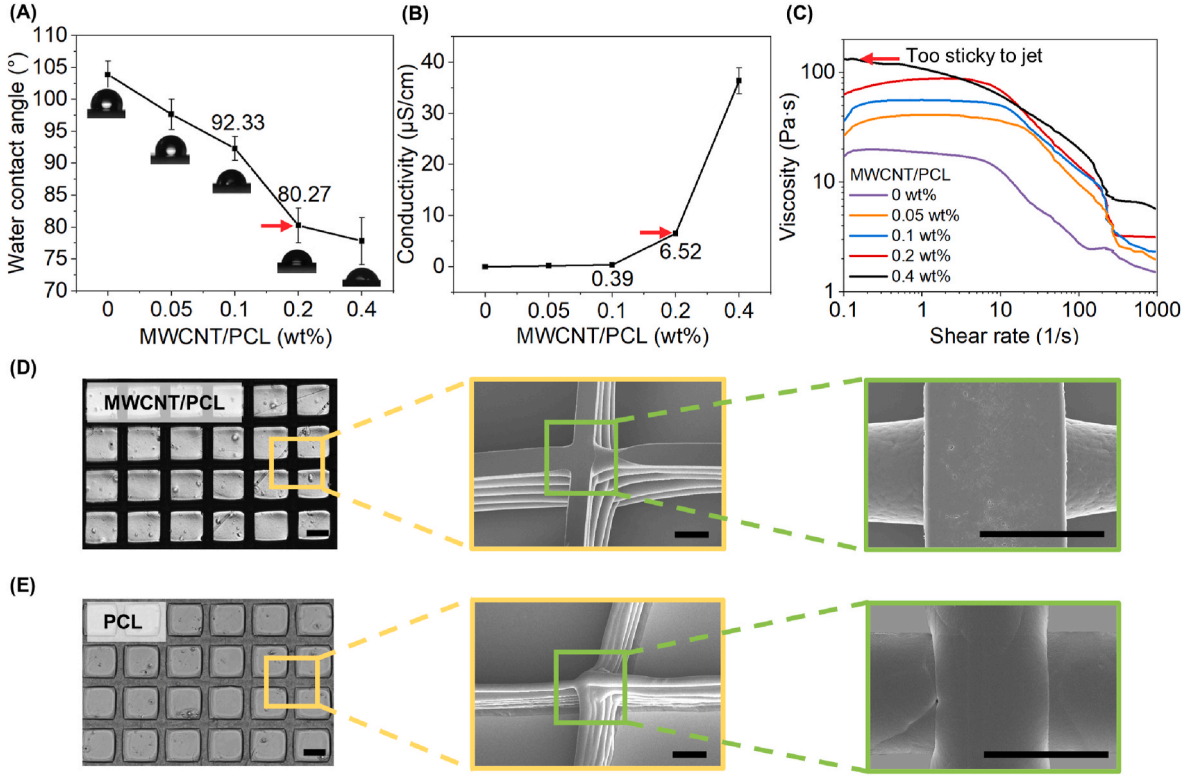

Fig. 2. Material properties characterization. (A) Contact angle of MWCNT/PCL with different ratios. (B) Conductivity of MWCNT/PCL with different ratios. (C) Variation curve of viscosity with the shear rate for different ratios of MWCNT/PCL. (D) Microscope and SEM micrographs of MWCNT/PCL (0.2 wt%) grid printed by electrowriting. Scale bar = 50 μm. (E) Microscope and SEM micrographs of PCL grid printed by electrowriting. Scale bar = 50 μm.

the good printability of MWCNT/PCL in this printing method (Fig. S1).

3.1.3. Biocompatibility evaluation of MWCNT/PCL and PCL patterns

Madin-Darby canine kidney (MDCK) cells were seeded and cultured on MWCNT/PCL and PCL SL patterns for 3 days. The MWCNT/PCL and PCL SL patterns were single layer fibers, at which point the cells were able to cross the lines to have more contact with the material and to better validate biocompatibility. Cell cytoskeleton and nucleus were stained by FITC phalloidin and 4',6-diamidino-2-phenylindole (DAPI), respectively. Staining images revealed that the cell morphology on MWCNT/PCL and PCL was normal and similar (Fig. 3A). The cytocompatibility of MWCNT/PCL and PCL was evaluated by CCK-8 on days 1, 2, and 3 after cell seeding. The results demonstrated that cells proliferated significantly faster on MWCNT/PCL substrates on day 2, but there was no significant difference on day 3, indicating that both materials were nontoxic to cells (Fig. 3B). Furthermore, cell spreading areas decreased as cell density increased in all substrates. Cells had a significantly larger spreading area in MWCNT/PCL SL than the PCL one on days 1 and 2, which may be attributed to the higher hydrophilicity of MWCNT/PCL.

3.2. Cell migration under electrical and topographic stimulations

3.2.1. Cell migration on a planar substrate with different EF strengths

In cell migration experiment, multilayer straight lines were used to ensure the cells were barely able to cross the straight line. In the incubator, a time-lapse monitoring device was used to observe cell migration, and the basic quantities of cell migration were defined (Fig. 4A). EF was added by inserting Pt electrodes into the culture medium directly, offering a more convenient method than using a salt bridge [31,32]. In addition to being more convenient, it's also because MDCK cells show electrotaxis at small electric fields and there is little difference in cell damage between the salt bridge system and direct electrical stimulation at small electric fields. Moreover, the salt bridge system has another disadvantage: the voltage varies with the reduction of ionic movement in the salt bridge. However, the limitation of the electrical stimulated device was that EF cannot exceed 1.2 V cm^{-1} due to the electrode-induced medium ionization that will cause cell death according to the experiments.

Cell migration speed first increased and then decreased with the increase of EF, and cell migration direction was random until EF reached 1 V cm^{-1} (Fig. 4B; Video S2 and S3). Cells migrated toward the cathode when EF surpassed 1 V cm^{-1}, consistent with previous research [33]. Thus, EF strength must exceed 1 V cm^{-1} to regulate cell migration direction; at this threshold, cell migration speed remains superior to the situation without EF.

3.2.2. Cell migration on the combined stimulation of conductive/nonconductive SL and EF

To investigate cell migration under varying combined stimulations of EF and SL, and the influence of pattern conductivity, conductive (MWCNT/PCL) and nonconductive (PCL) SL with a 50 μm spacing were printed as stimulating topography, and the stimulated EF was set as 1 V cm^{-1}. There were three distinct experimental sets according to the various combinations of EF and SL direction, namely, SL without EF (NEF), SL perpendicular to EF (perpendicular), and SL parallel to EF (parallel), and each SL with conductive and nonconductive materials (Videos S4-S9). The bright-field images of cells on MWCNT/PCL (Fig. 4C–i) and PCL SL were captured (Fig. S2).

The distribution of the cell migration angle demonstrated that cells migrated along SL in PCL and MWCNT/PCL groups when there was no EF (Fig. 4C–ii). When SL was perpendicular to EF, cells migrated along SL when SL was nonconductive but migrated along EF when SL was conductive, and cells were forced to redirect migration direction when they reached the boundaries. When SL was parallel to EF, cell migration angles showed no significant differences between MWCNT/PCL and PCL groups due to the same guidance direction of EF and SL. In summary, in either case, SL always limit the direction of cell migration if the height of SL is sufficiently high, which is better understood from an energetic standpoint (need to overcome gravity to cross the obstruction). Cell migration trajectories (Fig. S3A) and quantitative characterization data cosθ (Fig. S3B) also proved the above statement.

The migration speed in each experiment was calculated and compared (Fig. 4D). Cell migrated fastest when EF was parallel to conductive SL. Notably, cells migrated faster in each conductive group than the nonconductive one in all cases, indicating the importance of the

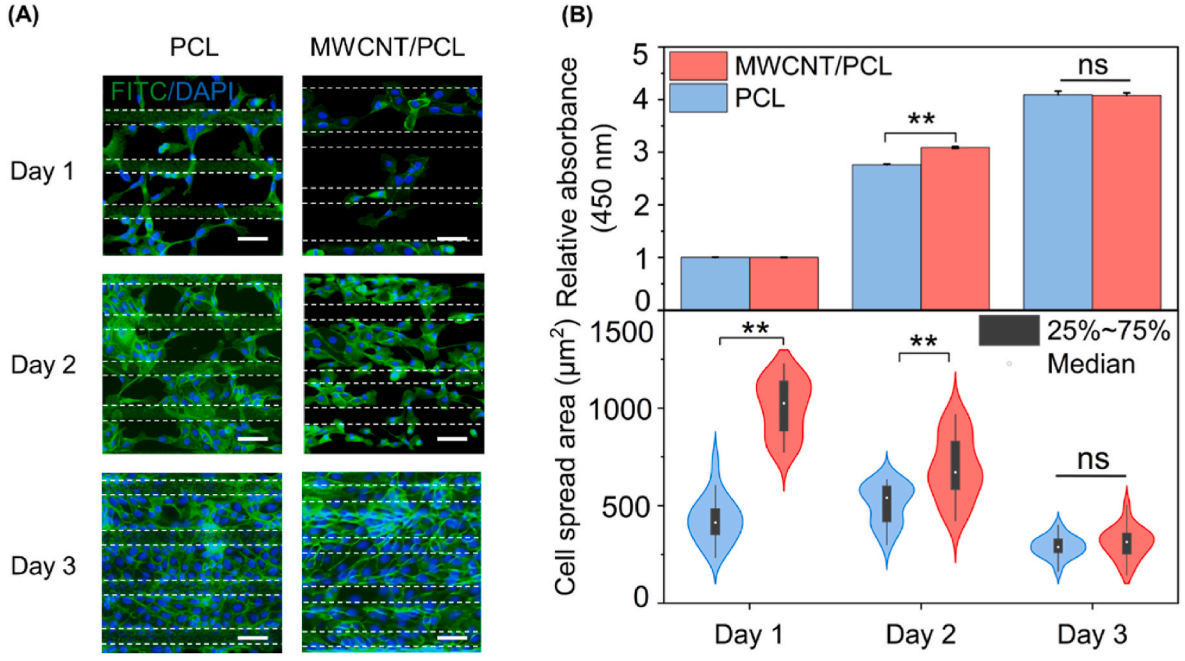

Fig. 3. Biocompatibility testing of materials. (A) Cytoskeleton staining images of MDCK cells after culturing on PCL and MWCNT/PCL SL for days 1, 2, and 3 (green: FITC, blue: DAPI). Scale bar = 50 μm. (B) Proliferation (CCK-8 assay) and cell spreading area on different substrates for days 1, 2, and 3.

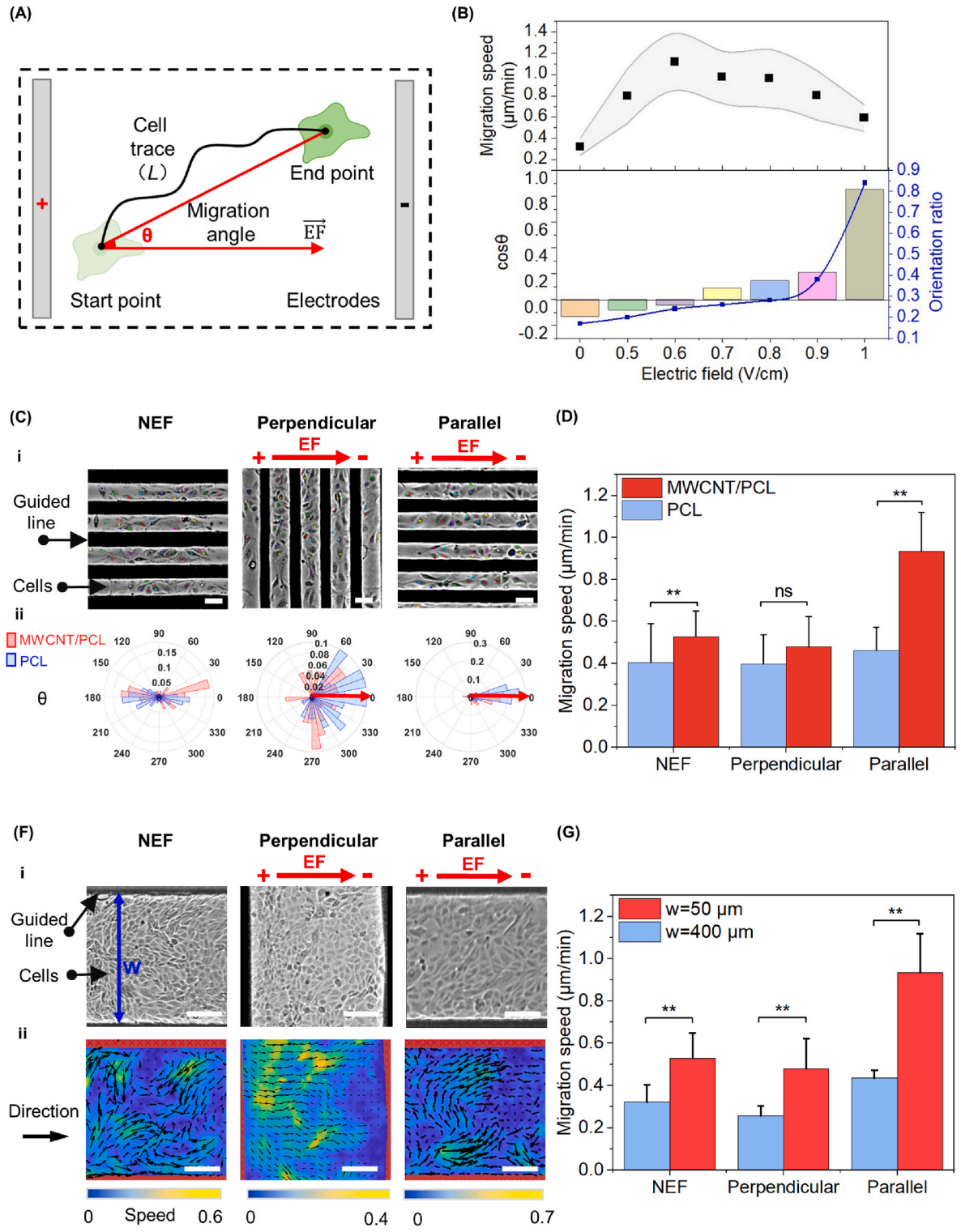

Fig. 4. Cell migration under the different physical factor stimulation. (A) Definition of basic quantities of cell migration. (B) Migration speed and direction (cosθ and orientation ratio) of cells in the plane at different strengths of electric fields. (C) (i) Experimental images of cells migrated under the combination guidance of conductive (MWCNT/PCL) straight lines and electric fields. Scale bar = 50 μm. (ii) Comparison of cell migration angle under the conductive (MWCNT/PCL) or nonconductive (PCL) straight lines and electric fields stimulation (conductive: red, nonconductive: blue). (D) Comparison of cell migration speed under the guidance of conductive (MWCNT/PCL) or nonconductive (PCL) straight lines and electric fields. (F) (i) The experimental images of cell migration are guided by a combination of wide conductive straight lines and electric fields. Scale bar = 100 μm. (ii) Cell migration direction and velocity field obtained by PIVlab analysis. Scale bar = 100 μm. (G) Comparison of cell migration speed under the guidance of wide/narrow straight lines and electric fields.

conductivity of the material. Reasons for this phenomenon is probably because conductive fibers were more hydrophilic, and cells preferred to adhere and migrate on hydrophilic surfaces [34,35]. Another reason for the differences between PCL and MWCNT/PCL SL was that EF strength between conducting and nonconducting fibers was different when the same EF was applied, as verified by finite element analysis (FEA; Fig. S4). FEA results denoted that the effective EF between conductive fibers was greater than that between nonconductive fibers when the same EF was applied, indicating that cells between conductive fibers were subjected to a stronger EF. Moreover, tiny currents on conducting fibers may also lead to increased cell migration speed. Interestingly, in conductive and nonconductive groups, the cell migration speed was greater in the parallel group than in the NEF group than in the perpendicular group, which may be caused by SL and EF guided cell migrated toward the same direction in the parallel one, whereas guided directions of SL and EF were reversed and impeded each other in perpendicular.

3.2.3. Cell migration on the combined stimulation of narrow/wide-spacing SL and EF

SL spacing has a significant effect on cell migration [36]. Groove spacing ranging from 200 nm to 100 μm can enhance cell migration speed and directionality, and the increase in cell migration speed is more pronounced when the groove spacing is close to the cell size [37–39]. Therefore, to investigate the influence of fiber spacing, narrow-spacing (50 μm) SL, which is slightly larger than the size of MDCK cells (~15 μm), and wide-spacing (400 μm) SL, which is much larger than the cellular scale, were chosen and compared (Fig. 4F–i). PIVlab, a MATLAB application, was employed to analyze the cell migration direction and speed distribution between the wide-spacing SL (Fig. 4F–ii). Cells migrated randomly between the wide-spacing SL in the absence of EF, and cells migrated along with EF regardless of the SL direction, indicating that the wide-spacing SL cannot direct cell migration (Videos S10-S12). The qualitative and quantitative comparison of cell migration direction in wide and narrow-spacing SL revealed that narrow-spacing SL has more impact on cell migration direction (Fig. S5). Moreover, the comparison of cell migration speed revealed that cells migrated in narrow grooves were significantly faster than those in wide grooves, and the difference among the NEF, parallel, and perpendicular groups was more pronounced within the narrow-spacing group, further confirming that narrow-spacing SL has more impact on cell migration (Fig. 4G). Above results underscores the pivotal role of fiber spacing in governing cell migration speed and directionality.

3.3. Cell migration model and validation

Existing physical models that describe cell migration on different substrate topographies have various limitations, such as modeling cells simplistically [40], numerous training data needed [41], and only considering the substrate as a drag force provider, neglecting the effects of shapes [42]. Most models describe the cell as a charged sphere in an EF to analyze cell interactions with EF [43,44]. However, there are no physical models to describe and analyze cell migration under simultaneous stimulation of EF and substrate topography. A model is urgently needed to explain and simulate cell migration under dual-factor stimulation [45].

A model based on the particle-based compass model in reference was developed, which simulated cell migration according to intercellular interaction, to capture the underlying mechanism of cell migration under the combined stimulation of SL and EF (Fig. 5A) [29]. The variation of cell migration speed and orientation ratio with the strength of EF was fitted and assigned as the model setup (Fig. S6). The model's validity was first verified by simulating cell migration in the plane with EF (1 V cm^{-1}) and NEF (Videos S13 and S14). Comparative analysis of the cell migration speed and angle in experiments and simulations demonstrated consistency in all scenarios, indicating the model's validity (Fig. 5B and C; Fig. S7).

Subsequently, boundary conditions were encompassed to simulate cell migration under the concurrent influence of narrow-spacing SL and EF, which involved NEF, SL with perpendicular EF, and SL with parallel EF (Videos S15-S17). Simulated results were represented in blue, whereas the experimental ones were in red. Notably, the simulated migration angle corresponds well to the experiment in all situations (Fig. 5D–i). Furthermore, cell migration speed on narrow-spacing SL was also simulated and compared to the experiment, and the value was still close to the experiment (Fig. S8).

Finally, cell migration guided by wide-spacing SL and EF was simulated. There were also three conditions: NEF, SL with perpendicular EF, and SL with parallel EF (Videos S18-S20). The migration angle (Fig. 5D–ii) and speed (Fig. 5D–iii) at different points of the cross-sections obtained from experiments and simulations were marked in red and blue, respectively. Cell migration angle and speed distribution in the cross-sections in the model corresponded well with that in the experiments. In NEF and SL parallel to EF, cell migration was faster in locations close to the fibers and slower in intermediate regions. When SL was perpendicular to EF, the local cell migration speed decreased along the electric potential direction. In summary, experiments and simulations corresponded well in all scenarios, indicating that the model is effective.

Nevertheless, this model still has some limitations; for instance, it cannot characterize cell migration in three-dimensional (3D) space, neglects cell-to-cell information exchange and collecting cellular effects, and lacks correspondence to biological mechanisms. Current studies on the biological mechanism suggest that cells sense EF through membrane depolarization and electromigration of surface proteins [46]. Multiple signaling pathways, proteins, and genes are involved in sensing and reaction to electrical stimulation, such as AKT, Src-family kinases, MEK-ERK, JAK1 [47], PI3K [48], ERK1/2 [49], PI3K/mTOR/AKT [50], gefA, rasC, rip3, Ist8, and pkbR1 [51], KCNJ15, Kir4.2 [52], and so on. Additionally, the intercellular bond strength also affects the electrotaxis of epithelial cells: a stronger interaction leads to weaker electrotaxis [53]. Cells sense substrate topography by other protein and signaling pathways, such as Arp2/3, POPX2, PI3K, ROCK, and so on [14,54]. However, a scarcity of studies bridges molecular mechanisms and macroscopic physical models [55]. Consequently, extending the physical model on 3D space, considering migration decisions due to cell-to-cell information exchange, and modeling cell migration based on biological mechanisms may be the next step.

3.4. In vivo wound healing assay

To further confirm the synergistic effects of EF and guided topographic pattern *in vivo*, a mouse skin wound model was established (Fig. 6A). The printed patterns are sterilized and applied directly to the wound, the electrodes are then covered with the material and finally fixed with medical tape (Fig. S9). The experiment was divided into four groups: control (without guided pattern and EF), PCL (nonconductive guided pattern, without EF), MWCNT/PCL (conductive guided pattern, without EF), and MWCNT/PCL + EF (conductive guided pattern, with EF) (Fig. 6B). Guided patterns were grid membranes, and EF was 1 V cm^{-1}.

Wounds were created on day 0 and photographed on days 0, 3, 7, and 14 for wound-healing area assessment, and histopathological evaluation of wound regeneration status on day 14 was performed by hematoxylin and eosin (H&E) staining (Fig. 6C). The most effective healing occurred in the MWCNT/PCL + EF group, followed by the MWCNT/PCL, PCL, and control groups (Fig. 6D). On days 3, 7, and 14, the wound healing rate in the MWCNT/PCL + EF group was significantly higher than that in the control and PCL groups ($P < 0.05$), and slightly greater than that in the MWCNT/PCL group without significantly differences. The wound-healing rate in the PCL group was slightly greater than that in the control without significant differences. These findings suggested that

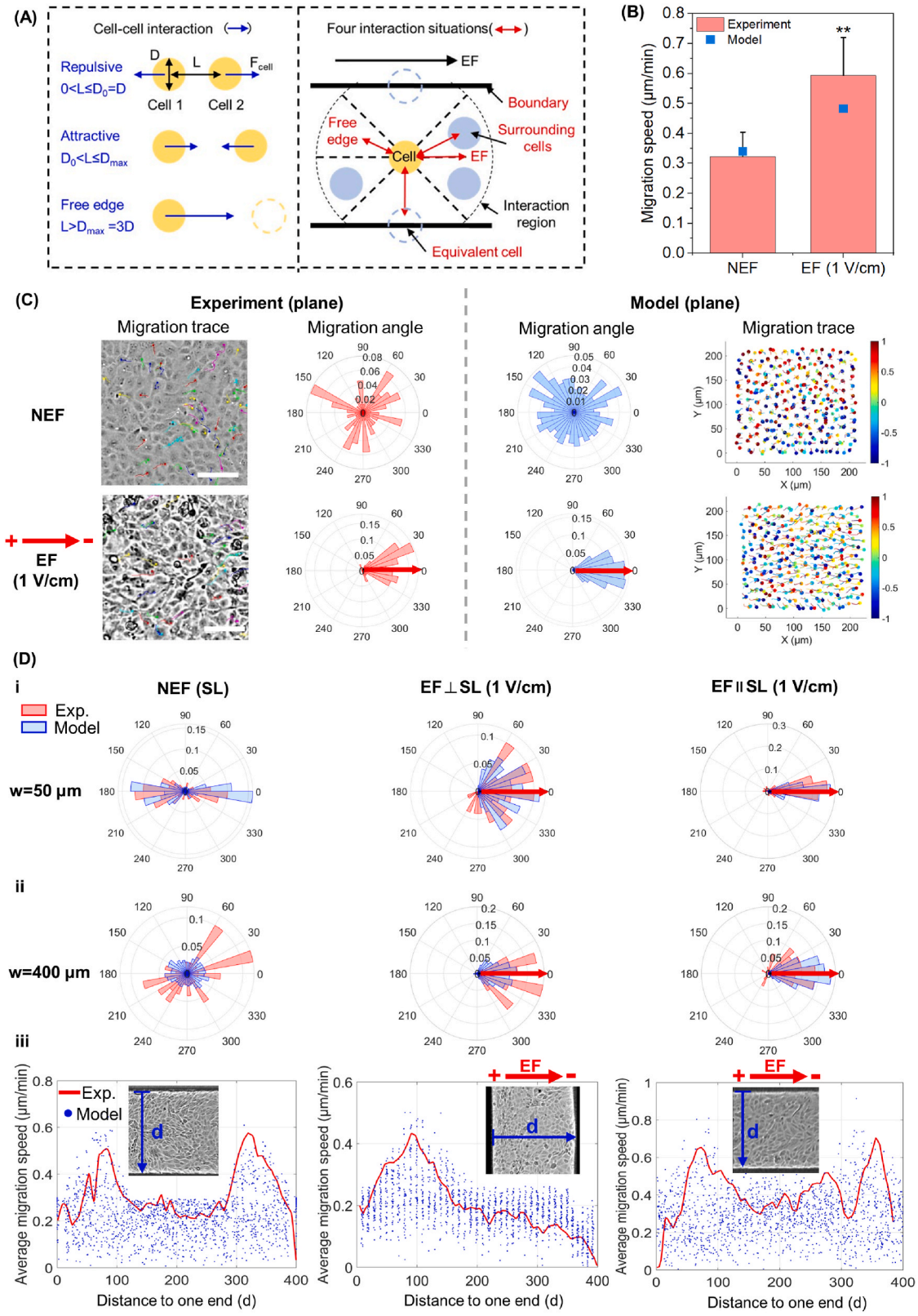

Fig. 5. Comparison of cell migration in experiment and model. (A) Schematic diagram of the mechanism of the model. (B) Comparison of cell migration speed under the stimulation of NEF and EF (1 V/cm) in planar substrate in experiment and model. (C) Comparison of cell migration track and angular distribution under the stimulation of NEF and EF (1 V/cm) in the plane in experiment and model (experiment: red, model: blue). Scale bar = 100 μm. (D) (i) Comparison of cell migration angular distribution in narrow straight lines without the EF, with perpendicular EF, and with parallel EF in experiment and model (experiment: red, model: blue). (ii) Comparison of cell migration angular distribution in wide straight lines without the EF, with perpendicular EF, and with parallel EF in experiment and model. (iii) Comparison of cell migration speed distribution with distance to one end (d) in wide straight lines without the EF, with perpendicular EF, and with parallel EF in experiment and model.

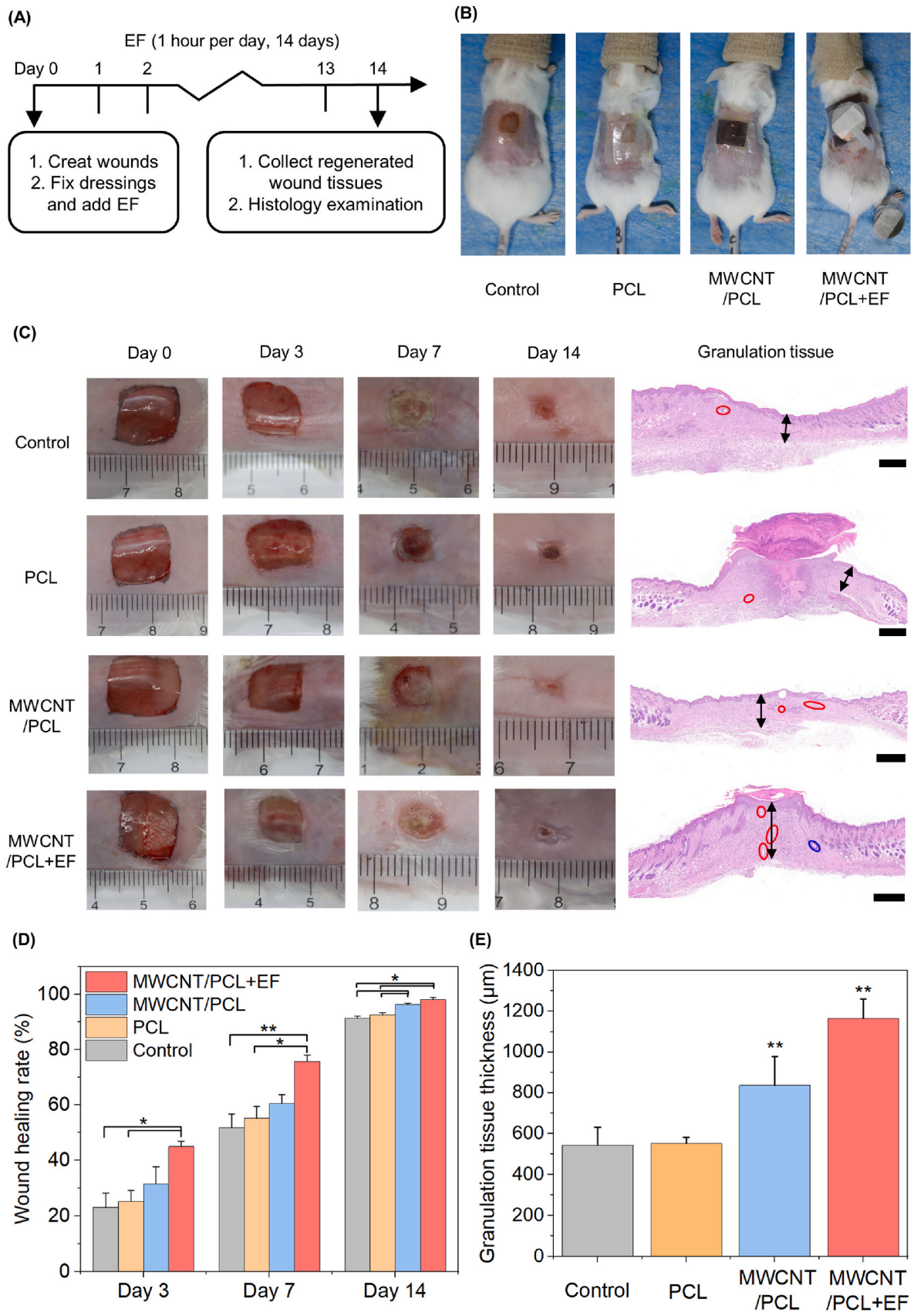

Fig. 6. *In vivo* wound healing assay. (A) Schematic diagram of the schedule of *in vivo* wound healing assay. (B) Images of experiments with different groups. (C) Photographs of wounds on days 0, 3, 7, and 14, and H&E staining on day 14 from the different groups (granulation tissue: black arrow, newly formed blood vessel: red circle, hair follicles: blue circle). Scale bar = 500 μm. (D) Comparison of wound healing area for each group on days 3, 7, and 14. (E) Comparison of granulation tissue thickness for each group on day 14.

although substrate topography played a role in promoting wound healing, its impact was overshadowed by the influence of electrical stimulation. This phenomenon may be attributed to the intricate nature of cell migration during wound healing, where cells not only migrate from the surroundings but also from deeper layers [5]. The designed topographic structures cannot induce upward cell migration from deeper layers, emphasizing the potential for future designs involving 3D-induced topographic structures to facilitate cell migration in multiple directions.

Moreover, histological evaluation results demonstrated that the thickness of the wound granulation tissue in the MWCNT/PCL + EF group was greater than that in the MWCNT/PCL group, followed by the PCL and control groups (Fig. 6E). The MWCNT/PCL + EF and MWCNT/PCL groups significantly differed from the other groups ($P < 0.01$), whereas no significant difference emerged between the PCL and the control. Moreover, the MWCNT/PCL + EF group exhibited plentiful blood vessels and few hair follicles, indicating its beneficial effects on wound healing. In summary, these findings underscored the combined stimulation of EF and substrate topography in promoting wound healing, emphasizing their potential therapeutic applications.

4. Conclusion

This study explored cell migration under the combined stimulation of EF and substrate topography. Conductive (MWCNT/PCL) and nonconductive (PCL) SL with narrow (50 μm) and wide (400 μm) spacing were fabricated by electrowriting as stimulated topography. Cell migration was studied under several stimulated conditions, including different direction combinations of EF and SL, with distinct SL conductivity and spacing. Cells migrated faster with more directivity between the narrow-spacing SL than the wide-spacing one, and cells migrated faster in the conductive SL regardless of the direction combination of EF and SL. Cell migration speed first increased and then decreased as the strength of EF increased, and it displayed electrotaxis until EF reached 1 V cm^{-1}. Cell migration speed and directivity were the greatest when EF was parallel to conductive narrow-spacing SL. When EF was perpendicular to narrow-spacing SL, cell migration direction depended on the material's conductivity. Wide-spacing SL exerted a negligible impact on the average cell migration speed. Subsequently, a model based on intercellular interactions was developed to describe and predict cell migration under the guidance of SL and EF, which corresponded well with experimental results in all conditions. Next, *in vivo* skin wound healing experiments revealed that EF (1 V cm^{-1}) parallel to conductive guided substrate significantly enhanced the wound-healing rate and granulation tissue thickness. This study investigated cell migration under synergistic electrical and topographic stimulations, providing new insights into guiding cell migration and promoting wound healing.

CRediT authorship contribution statement

Huinan Lai: Writing – review & editing, Writing – original draft, Visualization, Software, Resources, Project administration, Methodology, Investigation, Formal analysis, Data curation, Conceptualization. **Xiaodan Huo:** Writing – review & editing, Methodology, Investigation, Formal analysis, Data curation. **Ying Han:** Writing – review & editing, Methodology, Formal analysis, Data curation. **Minyu Hu:** Writing – review & editing, Methodology. **Xiangren Kong:** Writing – review & editing, Formal analysis, Data curation. **Jun Yin:** Writing – review & editing, Supervision, Funding acquisition, Conceptualization. **Jin Qian:** Writing – review & editing, Supervision, Methodology, Funding acquisition, Conceptualization.

Declaration of competing interest

The authors declare that they have no known competing financial interests or personal relationships that could have appeared to influence the work reported in this paper.

Data availability

Data will be made available on request.

Acknowledgements

This work was supported by the National Natural Science Foundation of China (Grant Numbers: 12125205, 12072316, 12132014, and 52075482), the Key Research and Development Program of Zhejiang Province (2021C01183), and the Zhejiang Provincial Natural Science Foundation of China (LD22A020001). We would like to thank Professor Daniel Cohen of Princeton University for giving us some suggestions about improving the electrical stimulation devices.

Appendix A. Supplementary data

Supplementary data to this article can be found online at https://doi.org/10.1016/j.mtbio.2024.101083.

References

[1] E.M. Tottoli, R. Dorati, I. Genta, E. Chiesa, S. Pisani, B. Conti, Skin wound healing process and new emerging technologies for skin wound care and regeneration, Pharmaceutics 12 (2020) 735, https://doi.org/10.3390/pharmaceutics12080735.
[2] R. Luo, J. Dai, J. Zhang, Z. Li, Accelerated skin wound healing by electrical stimulation, Adv. Healthcare Mater. 10 (2021) 2100557, https://doi.org/10.1002/adhm.202100557.
[3] R. Li, K. Liu, X. Huang, D. Li, J. Ding, B. Liu, X. Chen, Bioactive materials promote wound healing through modulation of cell behaviors, Adv. Sci. 9 (2022) 2105152, https://doi.org/10.1002/advs.202105152.
[4] S. Martinotti, E. Ranzato, Scratch wound healing assay, Epidermal Cells Methods Protoc (2020) 225–229, https://doi.org/10.1007/7651_2019_259.
[5] H. Sorg, D.J. Tilkorn, S. Hager, J. Hauser, U. Mirastschijski, Skin wound healing: an update on the current knowledge and concepts, Eur. Surg. Res. 58 (2017) 81–94, https://doi.org/10.1159/000454919.
[6] M. Verdes, K. Mace, L. Margetts, S. Cartmell, Status and challenges of electrical stimulation use in chronic wound healing, Curr. Opin. Biotechnol. 75 (2022) 102710, https://doi.org/10.1016/j.copbio.2022.102710.
[7] Y. Zhang, X. Wang, Y. Zhang, Y. Liu, D. Wang, X. Yu, H. Wang, Z. Bai, Y. Jiang, X. Li, Endothelial cell migration regulated by surface topography of poly (ε-caprolactone) nanofibers, ACS Biomater. Sci. Eng. 7 (2021) 4959–4970, https://doi.org/10.1021/acsbiomaterials.1c00951.
[8] L. Ge, L. Yang, R. Bron, J.K. Burgess, P. van Rijn, Topography-mediated fibroblast cell migration is influenced by direction, wavelength, and amplitude, ACS Appl. Bio Mater. 3 (2020) 2104–2116, https://doi.org/10.1021/acsabm.0c00001.
[9] J. Vasudevan, K. Jiang, J.G. Fernandez, L.C. Teck, Extracellular matrix mechanobiologyin cancer cell migration, Acta Biomater. (2022), https://doi.org/10.1016/j.actbio.2022.10.016.
[10] S. Arora, S. Lin, C. Cheung, E.K.F. Yim, Y.-C. Toh, Topography elicits distinct phenotypes and functions in human primary and stem cell derived endothelial cells, Biomaterials 234 (2020) 119747, https://doi.org/10.1016/j.biomaterials.2019.119747.
[11] S.-H. Jeong, Y. Lee, M.-G. Lee, W.J. Song, J.-U. Park, J.-Y. Sun, Accelerated wound healing with an ionic patch assisted by a triboelectric nanogenerator, Nano Energy 79 (2021) 105463, https://doi.org/10.1016/j.nanoen.2020.105463.
[12] X. Zhang, G. Chen, L. Sun, F. Ye, X. Shen, Y. Zhao, Claw-inspired microneedle patches with liquid metal encapsulation for accelerating incisional wound healing, Chem. Eng. J. 406 (2021) 126741, https://doi.org/10.1016/j.cej.2020.126741.
[13] B. Cortese, I.E. Palamà, S. D'Amone, G. Gigli, Influence of electrotaxis on cell behaviour, Integr. Biol. 6 (2014) 817–830, https://doi.org/10.1039/c4ib00142g.
[14] H. Lai, B. Gong, J. Yin, J. Qian, 3D printing topographic cues for cell contact guidance: a review, Mater. Des. (2022) 110663, https://doi.org/10.1016/j.matdes.2022.110663.
[15] A.A. Vu, D.A. Burke, A. Bandyopadhyay, S. Bose, Effects of surface area and topography on 3D printed tricalcium phosphate scaffolds for bone grafting applications, Addit. Manuf. 39 (2021) 101870, https://doi.org/10.1016/j.addma.2021.101870.
[16] B. Wang, J. Shi, J. Wei, X. Tu, Y. Chen, Fabrication of elastomer pillar arrays with elasticity gradient for cell migration, elongation and patterning, Biofabrication 11 (2019) 45003, https://doi.org/10.1088/1758-5090/ab21b3.
[17] L. Brigo, A. Urciuolo, S. Giulitti, G. Della Giustina, M. Tromayer, R. Liska, N. Elvassore, G. Brusatin, 3D high-resolution two-photon crosslinked hydrogel structures for biological studies, Acta Biomater. 55 (2017) 373–384, https://doi.org/10.1016/j.actbio.2017.03.036.
[18] M. Ottosson, A. Jakobsson, F. Johansson, Accelerated wound closure-differently organized nanofibers affect cell migration and hence the closure of artificial

wounds in a cell based *in vitro* model, PLoS One 12 (2017) e0169419, https://doi.org/10.1371/journal.pone.0169419.
[19] C. Wang, Y. Xu, J. Xia, Z. Zhou, Y. Fang, L. Zhang, W. Sun, Multi-scale hierarchical scaffolds with aligned micro-fibers for promoting cell alignment, Biomed. Mater. 16 (2021) 45047, https://doi.org/10.1088/1748-605X/ac0a90.
[20] M. Werner, A. Petersen, N.A. Kurniawan, C.V.C. Bouten, Cell-perceived substrate curvature dynamically coordinates the direction, speed, and persistence of stromal cell migration, Adv. Biosyst. 3 (2019) 1900080, https://doi.org/10.1002/adbi.201900080.
[21] X. Lei, S. Miao, X. Wang, Y. Gao, H. Wu, P. Cheng, Y. Song, L. Bi, G. Pei, Microgroove cues guiding fibrogenesis of stem cells via intracellular force, ACS Appl. Mater. Interfaces 15 (2023) 16380–16393, https://doi.org/10.1021/acsami.2c20903.
[22] I.M. Handrea-Dragan, I. Botiz, A.-S. Tatar, S. Boca, Patterning at the micro/nano-scale: polymeric scaffolds for medical diagnostic and cell-surface interaction applications, Colloids Surf. B Biointerfaces (2022) 112730, https://doi.org/10.1016/j.colsurfb.2022.112730.
[23] M.M. Nazemi, A. Khodabandeh, A. Hadjizadeh, Near-field electrospinning: crucial parameters, challenges, and applications, ACS Appl. Bio Mater. 5 (2022) 394–412, https://doi.org/10.1021/acsabm.1c00944.
[24] B.S. Eftekhari, M. Eskandari, P.A. Janmey, A. Samadikuchaksaraei, M. Gholipourmalekabadi, Surface topography and electrical signaling: single and synergistic effects on neural differentiation of stem cells, Adv. Funct. Mater. 30 (2020) 1907792, https://doi.org/10.1002/adfm.201907792.
[25] I. Jun, N. Li, J. Shin, J. Park, Y.J. Kim, H. Jeon, H. Choi, J.-G. Cho, B.C. Choi, H.-S. Han, Synergistic stimulation of surface topography and biphasic electric current promotes muscle regeneration, Bioact. Mater. 11 (2022) 118–129, https://doi.org/10.1016/j.bioactmat.2021.10.015.
[26] H.Y. Gong, J. Park, W. Kim, J. Kim, J.Y. Lee, W.-G. Koh, A novel conductive and micropatterned PEG-based hydrogel enabling the topographical and electrical stimulation of myoblasts, ACS Appl. Mater. Interfaces 11 (2019) 47695–47706, https://doi.org/10.1021/acsami.9b16005.
[27] J.-J. Lee, H.Y. Ng, Y.-H. Lin, E.-W. Liu, T.-J. Lin, H.-T. Chiu, X.-R. Ho, H.-A. Yang, M.-Y. Shie, The 3D printed conductive grooved topography hydrogel combined with electrical stimulation for synergistically enhancing wound healing of dermal fibroblast cells, Biomater. Adv. 142 (2022) 213132, https://doi.org/10.1016/j.bioadv.2022.213132.
[28] J. Wang, H. Wang, X. Mo, H. Wang, Reduced graphene oxide-encapsulated microfiber patterns enable controllable formation of neuronal-like networks, Adv. Mater. 32 (2020) 2004555, https://doi.org/10.1002/adma.202004555.
[29] Y. Zhang, G. Xu, J. Wu, R.M. Lee, Z. Zhu, Y. Sun, K. Zhu, W. Losert, S. Liao, G. Zhang, Propagation dynamics of electrotactic motility in large epithelial cell sheets, iScience 25 (2022), https://doi.org/10.1016/j.isci.2022.105136.
[30] J.C. Niple, J.P. Daigle, L.E. Zaffanella, T. Sullivan, R. Kavet, A portable meter for measuring low frequency currents in the human body, Bioelectromagn. J. Bioelectromagn. Soc. Soc. Phys. Regul. Biol. Med. Eur. Bioelectromagn. Assoc. 25 (2004) 369–373, https://doi.org/10.1002/bem.20000.
[31] J. Yang, X. Liu, W. Wang, Y. Chen, J. Liu, Z. Zhang, C. Wu, X. Jiang, Y. Liang, J. Zhang, Bioelectric fields coordinate wound contraction and re-epithelialization process to accelerate wound healing via promoting myofibroblast transformation, Bioelectrochemistry 148 (2022) 108247, https://doi.org/10.1016/j.bioelechem.2022.108247.
[32] S. Snyder, C. DeJulius, R.K. Willits, Electrical stimulation increases random migration of human dermal fibroblasts, Ann. Biomed. Eng. 45 (2017) 2049–2060, https://doi.org/10.1007/s10439-017-1849-x.
[33] T.J. Zajdel, G. Shim, L. Wang, A. Rossello-Martinez, D.J. Cohen, SCHEEPDOG: programming electric cues to dynamically herd large-scale cell migration, Cell Syst 10 (2020) 506–514, https://doi.org/10.1016/j.cels.2020.05.00910439-017-1849-x.
[34] L. Bacakova, E. Filova, M. Parizek, T. Ruml, V. Svorcik, Modulation of cell adhesion, proliferation and differentiation on materials designed for body implants, Biotechnol. Adv. 29 (2011) 739–767, https://doi.org/10.1016/j.biotechadv.2011.06.004.
[35] Y. Zhao, K. Yang, J. Li, Y. Huang, S. Zhu, Comparison of hydrophobic and hydrophilic intraocular lens in preventing posterior capsule opacification after cataract surgery: an updated meta-analysis, Medicine (Baltim.) (2017) 96, https://doi.org/10.1097/MD.0000000000008301.
[36] W. Liu, Q. Sun, Z. Zheng, Y. Gao, G. Zhu, Q. Wei, J. Xu, Z. Li, C. Zhao, Topographic cues guiding cell polarization via distinct cellular mechanosensing pathways, Small 18 (2022) 2104328, https://doi.org/10.1002/smll.202104328.
[37] S. Xiong, H. Gao, L. Qin, Y. Jia, M. Gao, L. Ren, Microgrooved collagen-based corneal scaffold for promoting collective cell migration and antifibrosis, RSC Adv. 9 (2019) 29463–29473, https://doi.org/10.1039/C9RA04009A.
[38] T. Wu, J. Xue, Y. Xia, Engraving the surface of electrospun microfibers with nanoscale grooves promotes the outgrowth of neurites and the migration of Schwann cells, Angew. Chem. Int. Ed. 59 (2020) 15626–15632, https://doi.org/10.1002/anie.202002593.
[39] C. Leclech, D. Gonzalez-Rodriguez, A. Villedieu, T. Lok, A.-M. Déplanche, A. I. Barakat, Topography-induced large-scale antiparallel collective migration in vascular endothelium, Nat. Commun. 13 (2022) 2797, https://doi.org/10.1038/s41467-022-30488-0.
[40] J.E. Dawson, T. Sellmann, K. Porath, R. Bader, U. van Rienen, R. Appali, R. Köhling, Cell-cell interactions and fluctuations in the direction of motility promote directed migration of osteoblasts in direct current electrotaxis, Front. Bioeng. Biotechnol. 10 (2022) 995326, https://doi.org/10.3389/fbioe.2022.995326.
[41] B. Sargent, M. Jafari, G. Marquez, A.S. Mehta, Y.-H. Sun, H. Yang, K. Zhu, R. R. Isseroff, M. Zhao, M. Gomez, A machine learning based model accurately predicts cellular response to electric fields in multiple cell types, Sci. Rep. 12 (2022) 9912, https://doi.org/10.1038/s41598-022-13925-4.
[42] P. Urdeitx, M.H. Doweidar, Enhanced piezoelectric fibered extracellular matrix to promote cardiomyocyte maturation and tissue formation: a 3D computational model, Biology 10 (2021) 135, https://doi.org/10.3390/biology10020135.
[43] J. Jiang, P. Smith, M.C.W. van Rossum, Electro-physiology models of cells with spherical geometry with non-conducting center, Bull. Math. Biol. 82 (2020) 1–12, https://doi.org/10.1007/s11538-020-00828-6.
[44] A. Amoddeo, Mathematical model and numerical simulation for electric field induced cancer cell migration, Math. Comput. Appl. 26 (2020) 4, https://doi.org/10.3390/mca26010004.
[45] T.P. Prescott, K. Zhu, M. Zhao, R.E. Baker, Quantifying the impact of electric fields on single-cell motility, Biophys. J. 120 (2021) 3363–3373, https://doi.org/10.1016/j.bpj.2021.06.034.
[46] S. SenGupta, C.A. Parent, J.E. Bear, The principles of directed cell migration, Nat. Rev. Mol. Cell Biol. 22 (2021) 529–547, https://doi.org/10.1038/s41580-021-00366-6.
[47] M. Zhao, B. Song, J. Pu, T. Wada, B. Reid, G. Tai, F. Wang, A. Guo, P. Walczysko, Y. Gu, Electrical signals control wound healing through phosphatidylinositol-3-OH kinase-γ and PTEN, Nature 442 (2006) 457–460, https://doi.org/10.1038/nature04925.
[48] G.M. Allen, A. Mogilner, J.A. Theriot, Electrophoresis of cellular membrane components creates the directional cue guiding keratocyte galvanotaxis, Curr. Biol. 23 (2013) 560–568, https://doi.org/10.1016/j.cub.2013.02.047.
[49] X. Ren, H. Sun, J. Liu, X. Guo, J. Huang, X. Jiang, Y. Zhang, Y. Huang, D. Fan, J. Zhang, Keratinocyte electrotaxis induced by physiological pulsed direct current electric fields, Bioelectrochemistry 127 (2019) 113–124, https://doi.org/10.1016/j.bioelechem.2019.02.001.
[50] J.G. Lyon, S.L. Carroll, N. Mokarram, R. V Bellamkonda, Electrotaxis of glioblastoma and medulloblastoma spheroidal aggregates, Sci. Rep. 9 (2019) 5309, https://doi.org/10.1038/s41598-019-41505-6.
[51] R. Gao, S. Zhao, X. Jiang, Y. Sun, S. Zhao, J. Gao, J. Borleis, S. Willard, M. Tang, H. Cai, A large-scale screen reveals genes that mediate electrotaxis in Dictyostelium discoideum, Sci. Signal. 8 (2015), https://doi.org/10.1126/scisignal.aab0562 ra50–ra50.
[52] K. Nakajima, K. Zhu, Y.-H. Sun, B. Hegyi, Q. Zeng, C.J. Murphy, J.V. Small, Y. Chen-Izu, Y. Izumiya, J.M. Penninger, KCNJ15/Kir4. 2 couples with polyamines to sense weak extracellular electric fields in galvanotaxis, Nat. Commun. 6 (2015) 8532, https://doi.org/10.1038/ncomms9532.
[53] G. Shim, D. Devenport, D.J. Cohen, Overriding native cell coordination enhances external programming of collective cell migration, Proc. Natl. Acad. Sci. USA 118 (2021) e2101352118, https://doi.org/10.1073/pnas.2101352118.
[54] J. Park, D.-H. Kim, A. Levchenko, Topotaxis: a new mechanism of directed cell migration in topographic ECM gradients, Biophys. J. 114 (2018) 1257–1263, https://doi.org/10.1016/j.bpj.2017.11.3813.
[55] K. Adebowale, Z. Gong, J.C. Hou, K.M. Wisdom, D. Garbett, H. Lee, S. Nam, T. Meyer, D.J. Odde, V.B. Shenoy, Enhanced substrate stress relaxation promotes filopodia-mediated cell migration, Nat. Mater. 20 (2021) 1290–1299, https://doi.org/10.1038/s41563-021-00981-w.